



Empirical Modeling of Tropospheric Delays and Uncertainty

Jungang Wang^{1,2}, Junping Chen^{1,3,4}, Yize Zhang¹

1. Shanghai Astronomical Observatory, Chinese Academy of Sciences, Shanghai 200030, China
2. Space Geodetic Techniques, GeoForschungsZentrum (GFZ), Potsdam 14473, Germany
5. 3. School of Astronomy and Space Science, University of Chinese Academy of Sciences, Beijing 100049, China
4. Shanghai Key Laboratory of Space Navigation and Positioning Techniques, Shanghai Astronomical Observatory, Chinese Academy of Sciences, Shanghai 200030, China

Correspondence to: Junping Chen (junping.chen@shao.ac.cn)

Abstract. Accurate modeling of troposphere delay is important for high-precision data analysis of space geodetic techniques, such as the Global Navigation Satellite System (GNSS). The empirical troposphere delay models provide zenith delays with an accuracy of 3 to 4 cm globally and do not rely on external meteorological input. They are thus important for providing a priori delays and serving as constraint information to improve the convergence of real-time GNSS positioning, and in the latter case, the proper weighting is critical. Currently, the empirical troposphere delay models only provide the delay value, but not the uncertainty of the delay. For the first time, we present a global empirical troposphere delay model, which provides both the zenith delay and the corresponding uncertainty, based on 10 years of tropospheric delays from the Numerical Weather Model (NWM). The model is based on a global grid, and at each grid point a set of parameters that describes the delay and uncertainty by the constant, annual, and semi-annual terms. The empirically modeled zenith delay has an agreement of 36 and 38 mm compared to three years delay values from NWM and four years estimates from GNSS stations, which is comparable to the previous models such as GPT3. The modeled ZTD uncertainty shows a correlation of 96% with the accuracy of the empirical ZTD model over 380 GNSS stations over the four years. For GNSS stations where the uncertainty annual amplitude is larger than 20 mm, the temporal correlation between the uncertainty and smoothed accuracy reaches 85%. Using GPS **pseudo**-kinematic PPP solutions of ~200 globally distributed stations over four months in 2020, we demonstrate that using the proper constraints can improve the convergence speed. The uncertainty modeling is based on a similar dataset as the GPT series, and thus it is also applicable for these empirical models.

25 1 Introduction

For space geodetic techniques such as Global Navigation Satellite System (GNSS), Very Long Baseline Interferometry (VLBI), and satellite altimetry, the microwave signals transmitting through the troposphere are delayed and bent due to the non-vacuum conditions of the troposphere, causing the tropospheric delay. The total tropospheric delay could be divided into the hydrostatic and wet parts. The former accounts for 90% of the total delay and is strongly dependent on the atmospheric pressure, and at 30 the height of sea level, it is around 2 meters in the zenith direction. The latter is closely related to the water vapor, and can hardly be modeled due to the unpredictability of water vapor in spatial and temporal. In data processing of these space geodetic techniques, the tropospheric delay is usually modeled as the zenith delay (zenith hydrostatic delay ZHD and zenith wet delay ZWD) and the mapping functions, and in high-precision applications, the horizontal gradients should also be considered (Böhm and Schuh, 2013).

35 Tropospheric zenith delay could be derived from in situ meteorological observations using the Saastamoinen or Hopfield function (Askne and Nordius, 1987; Hopfield, 1969; Saastamoinen, 1972), radiosonde observations which give the vertical profiles of meteorological data (Chen and Liu, 2016; Liou et al., 2001; Wu et al., 2019), numerical weather model (NWM) (Böhm et al., 2007; Kouba, 2007; Landskron and Böhm, 2017), and other instruments such as water vapor radiometer (Braun et al., 2003; Niell et al., 2001). Despite the relatively high accuracy of these models, that is, varying from 5 mm to 2 cm, all



40 these methods require accurate meteorological information, which is not always available for real-time GNSS users. Another option is the empirical tropospheric delay model, which aims to represent the tropospheric delay with a set of simplified parameters. The empirical tropospheric delay model usually only requires the user's location (latitude, longitude, and height) and time as input. Therefore, it has the advantage of being free of external data communication and easy to compute. However, the empirical models usually have an accuracy of 3 to 5 cm with respect to NWM or GNSS estimates, depending on the
45 resolution of the model and more importantly, the water vapor content of the location (Böhm et al., 2015; Ding and Chen, 2020; Kos et al., 2009; Li et al., 2014; Penna et al., 2001; Yao et al., 2016; Yao et al., 2015)

The empirical tropospheric delay models are usually based on radiosonde observations (Leandro et al., 2007) or NWM-derived products (Böhm et al., 2015; Lagler et al., 2013; Landskron and Böhm, 2017; Li et al., 2012; Yao et al., 2015), and the zenith hydrostatic and wet delays are provided via global grids, spherical harmonic functions, or look-up tables. In the Global Pressure
50 and Temperature (GPT) models (Böhm et al., 2015; Kouba, 2009; Lagler et al., 2013; Landskron and Böhm, 2017), atmospheric pressure, temperature, and water vapor are provided given the location and time, and thus the zenith delays can be calculated using the Saastamoinen (Saastamoinen, 1972) and Asknew & Nordius (Askne and Nordius, 1987) equations. Unlike the GPT series which are based on the European Centre for Medium-Range Weather Forecasts (ECMWF) products, the TropGrid2 model is based on the National Center for Environmental Prediction (NCEP) product and directly provides
55 ZHD and ZWD instead of the meteorological parameters (Schüler, 2013). Similarly, the IGGtrop models are also based on the NCEP products and directly provide zenith delays (Li et al., 2014; Li et al., 2018; Li et al., 2012); the Global Zenith Tropospheric Delay (GZTD) models are based on the ECMWF-derived VMF products and provide zenith delay via a spherical harmonic function (Yao et al., 2016); the Improved Tropospheric Grid (ITG) model provides tropospheric delays and additional meteorological data (Yao et al., 2015). Slight improvements are reported with refined modeling methods, such as
60 including the diurnal periodical terms, adopting more complicated functions in modeling the altitude scaling, and increasing the spatial resolution (Hu and Yao, 2018; Huang et al., 2021; Huang et al., 2022; Mao et al., 2021; Sun et al., 2019; Wang et al., 2022; Xu et al., 2020; Zhou et al., 2022; Zhu et al., 2022). Chen et al. (2020) presented an empirical ZTD model over mainland China based on the GNSS ZTD estimates, and Li et al. (2021) combined radiosonde observations with NWM products to determine empirical meteorological models. The accuracy of these empirical models varies between 3 to 5 cm,
65 mainly depending on the references used for model evaluation, for example, the GNSS stations and radiosonde observations with different distributions.

Due to the correlation between receiver clocks, tropospheric parameters, and station coordinates, using accurate external tropospheric delay products with proper weighting can improve the convergence of Precise Point Positioning (PPP), especially in real-time applications where a fast convergence is of great interest. NWM-derived ZTD usually agrees with GNSS at the
70 level of 1 to 1.5 cm, and regional tropospheric delay modeling could reach an accuracy of below 1 cm, they are therefore used in enhancing real-time PPP convergence time (Cui et al., 2022; de Oliveira et al., 2016; Douša et al., 2018; Lu et al., 2017; Takeichi et al., 2009; Wilgan et al., 2017; Zhang et al., 2017; Zheng et al., 2017). In situ instruments such as water vapor radiometer and Raman lidar could provide high-precision tropospheric delays (within 1 cm) and are also investigated in improving precise GNSS data processing (Alber et al., 1997; Bock et al., 2001; Bosser et al., 2009; Wang and Liu, 2019; Ware
75 et al., 1993). It is also demonstrated that empirical tropospheric delay models can improve the convergence of GNSS PPP (Chen et al., 2020; Yao et al., 2017; Yao et al., 2014). Due to the different accuracies of these external tropospheric delay products, it is necessary to properly weight them when constrained in GNSS analysis. A too-tight constraint would introduce errors and degrade the accuracy of estimates, whereas a too-loose constraint can hardly contribute to reducing the convergence time. When using the NWM-derived or regional-modeled tropospheric delays, the weighting strategy is usually based on either
80 the statistic of a large number of stations or numerically tested criteria.

Currently, most empirical tropospheric delay models only provide the delay values, but not the uncertainty for these delays. Chen et al. (2020) proposed a regional empirical ZTD model based on GNSS ZTD estimates in the mainland China region



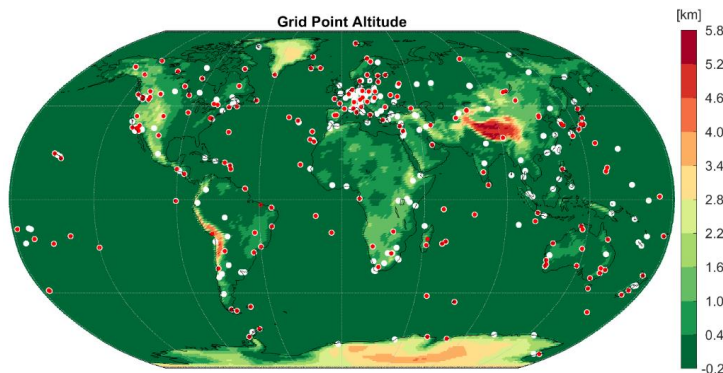
where formal errors are also provided. Motivated by using empirical tropospheric delay models in enhancing real-time GNSS positioning, in this work, we aim to provide both tropospheric delays and the corresponding uncertainties on a global scale.

85 We first fit the ZTD time series using the commonly adopted functions, that is, the constant plus annual and semi-annual periodical terms. The VMF ZTD global grids with a temporal resolution of $1^\circ \times 1^\circ$ in the period of 2009 to 2018 are used. After obtaining the fitting residuals at each grid point, we further model the squared residuals using a similar function as the ZTD modeling with only the constant and annual periodical terms. Eventually, we provide a set of coefficients that can present the zenith tropospheric delays and their uncertainty using a global grid, which can be used by real-time GNSS users to achieve 90 faster convergence. The model is evaluated using both NWM-derived delays over three years (2019–2021) and 380 GNSS stations over four years (2017–2020).

Following this introduction, we present the empirical modeling method and results of both ZTD and the corresponding uncertainties in Section 2. The model is evaluated using both NWM-derived tropospheric delays in Section 3 and GNSS ZTD estimates in Section 4. The impact of applying the model in kinematic PPP solutions is demonstrated in section 5. We 95 summarize the major findings and conclude this work in Section 6.

2 Empirical Modeling of ZTD and Uncertainty

In this work, the empirical modeling is based on the ZTD of the VMF3 operational tropospheric products (*Landskron and Böhm, 2017*), which is derived from the ECMWF NWM. The VMF3 tropospheric delay products are provided using a global grid with the spatial resolution of both $5^\circ \times 5^\circ$ and $1^\circ \times 1^\circ$, and we use the latter to obtain a better spatial resolution. The temporal 100 resolution is 6 hours, and we only use the epoch of 00:00 UTC. As we focus on the long-term signals of ZTD, including annual and semi-annual terms, the short-term fluctuations are smoothed out in the fitting, and, thus, taking one epoch per day does not affect our modeling results. More details about the VMF products can be found on the official website (<https://vmf.geo.tuwien.ac.at/>). We only give the ellipsoidal height of the grid points in Figure 1.



105 **Figure 1:** Altitude (ellipsoidal height) of the VMF3 grid points. The GNSS stations used for ZTD comparison and PPP validation are given in white and red dots, respectively.

2.1 Modeling of Zenith Total Delay

Following the previous works (Böhm et al., 2007; Böhm et al., 2015; Böhm et al., 2006; Lagler et al., 2013; Landskron and Böhm, 2017), at each grid point we first fit the ZTD value $ZTD(t)$ at epoch t using the following function, which considers constant, annual, and semi-annual terms.

$$ZTD(t) = Z_0 + Z_{s1} \sin\left(\frac{2\pi}{365.25}t\right) + Z_{c1} \cos\left(\frac{2\pi}{365.25}t\right) + Z_{s2} \sin\left(\frac{4\pi}{365.25}t\right) + Z_{c2} \cos\left(\frac{4\pi}{365.25}t\right) \quad (1)$$



115 Z_0 is the constant term which presents the average ZTD over a long term, Z_{s1} and Z_{c1} are the sine and cosine coefficients of the annual term, and Z_{s2} and Z_{c2} the sine and cosine coefficients of the semi-annual term. The epoch time t is given in Modified Julian Date (MJD).

120 Figure 2 gives the fitting results of the VMF ZTD products in the period of 2009 to 2018. As we do not model the diurnal variation, only the results of epoch 00:00 UTC is considered. The fitting residuals are related to both the altitude and latitude, and show regional patterns. On the one hand, the grid points with a higher altitude, for example, the Tibetan Plateau, Andes mountain, and the Antarctic, all have a smaller RMS value, mainly due to the less water vapor content at such a high altitude.

125 On the other hand, the RMS of fitting residuals also show a regional pattern. One example is the North Atlantic, where the RMS value around the Canary Current on the east side is much smaller than that around the Gulf Stream on the west side. The RMS value varies from 10 to 70 mm with 99% of the grid points within 60 mm (90% within 50 mm), and the average value is 36.0 mm. As for the average ZTD value, that is, the Z_0 term, it shows a strong dependence on the latitude and altitude of the grid points, especially the latter, mainly due to the distribution of atmospheric pressure. The value varies between 1100 mm in the high-altitude regions and 2700 mm in the tropical regions. The coefficients of the annual term have the opposite pattern in the North and South Hemispheres, especially the sine term, and that of the semi-annual term show more regional patterns.

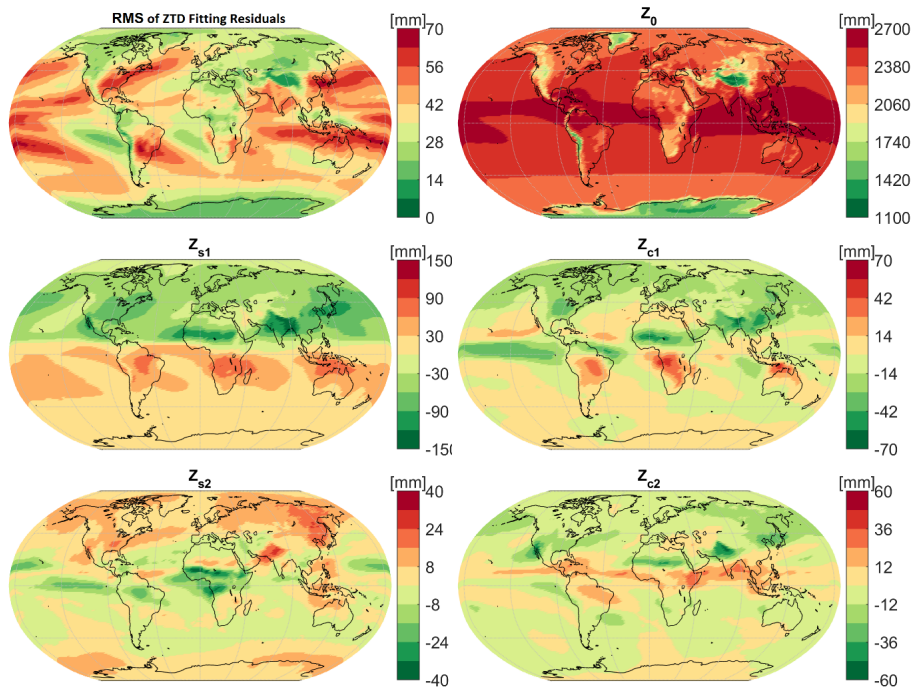
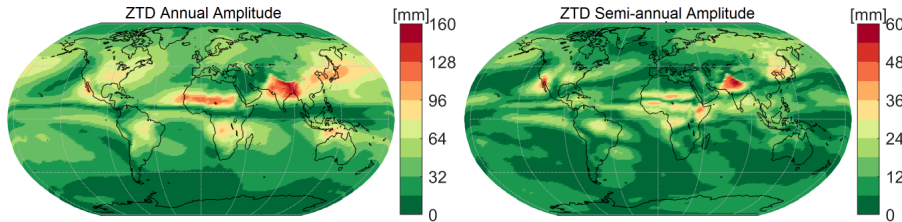


Figure 2: Fitting results of zenith total delay derived from the VMF global grid product from 2009 to 2018. Upper left: RMS of the ZTD fitting residuals. The rest subplots give the fitting coefficients of ZTD.

130 Note that we do not fit the ZTD time series with the function of amplitude A and initial phase φ , that is, $A \cdot \sin\left(\frac{2\pi}{365.25}t + \varphi\right)$. The reason is that without the coefficient of the initial phase, the fitting is numerically more stable. The initial phase and amplitude can always be retrieved given the sine and cosine coefficients, for example, the annual amplitude using $A_1 = \sqrt{s_1^2 + c_1^2}$. To better illustrate the annual and semi-annual variations of ZTD, we present the amplitude of the annual and semi-annual terms in Figure 3. The annual amplitude is less than 160 mm, and large values are observed in the north Indian subcontinent, between Sahara and Sub-Saharan Africa, and around Japan. The semi-annual amplitude is usually within 30 mm in most regions but extremely large values up to 60 mm also exist, which has a similar distribution as the large annual



amplitudes. The average value of annual and semi-annual amplitude on a global scale is 34.6 and 9.8 mm, respectively, and the 95% confidence interval is 78.4 and 22.2 mm.



140 **Figure 3: Annual (left) and semi-annual (right) amplitude from the numerical fitting of NWM-derived ZTD from 2009 to 2018.**

2.2 Modeling of ZTD formal error

Having the ZTD fitting residuals, that is, the ZTD from NWM-derived values minus that from the fitted values, we further model the formal errors $\sigma(t)$ (in the unit of mm) by fitting the squared ZTD residuals $Res(t)^2$ using the following equation, which considers constant, annual, and semi-annual periodical terms and minimizes the differences between the squared formal error and the squared ZTD residuals.

$$\Delta = \sigma(t)^2 - Res(t)^2$$
$$\sigma(t)^2 = R_0 + R_{s1} \sin\left(\frac{2\pi}{365.25}t\right) + R_{c1} \cos\left(\frac{2\pi}{365.25}t\right) + R_{s2} \sin\left(\frac{4\pi}{365.25}t\right) + R_{c2} \cos\left(\frac{4\pi}{365.25}t\right) \quad (2)$$

Similar to the ZTD modeling, R_0 gives the average value of the squared residuals over a long period, R_{s1} and R_{c1} are the sine and cosine coefficients of the annual term, and R_{s2} and R_{c2} are the sine and cosine coefficients of the semi-annual term. Δ is the difference between the squared formal error and the squared residuals of ZTD. Note that their units are all mm² given that the unit of the observations, that is, squared ZTD residuals $Res(t)^2$, is mm². We fit the squared residuals $Res(t)^2$ instead of the absolute value of ZTD residuals due to the following two reasons. First, the accuracy of tropospheric delay models is always evaluated by the root mean squares of the residuals, and numerically the statistic of absolute residuals is not equivalent to that of the RMS of the residuals, which means a scaling coefficient is required (Chen et al., 2020). Second, in enhancing GNSS positioning via constraining the tropospheric delay, the weighting of the tropospheric delay which serves as pseudo-range observation is based on the squared value of the formal error.

Figure 4 presents the fitting results of the squared ZTD residuals. The constant term R_0 follows the distribution of the RMS of ZTD residuals in Figure 2, as expected. Interestingly, the fitting accuracy of the ZTD residuals, that is, the upper left panel of Figure 4, also follows the distribution of the ZTD residuals. The spatial distribution of the annual and semi-annual periodical terms does not show an obvious correlation with the latitude or altitude of the grid points, and will be converted into amplitude in the following part and discussed there.

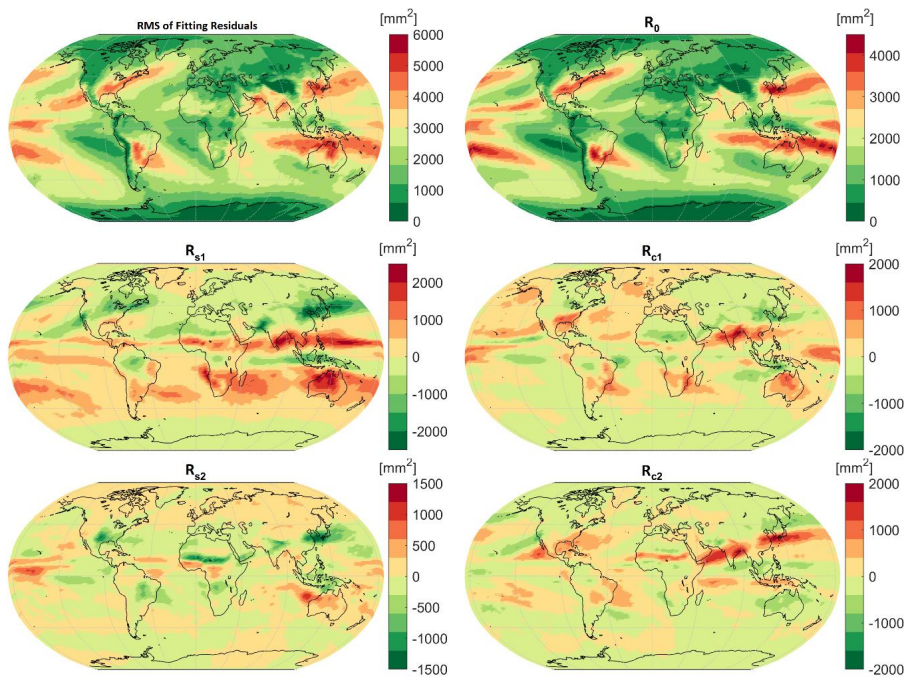
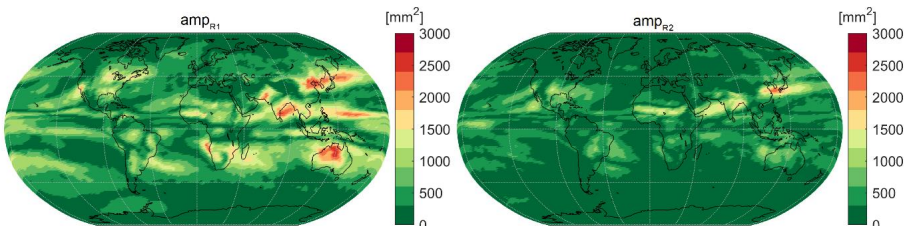


Figure 4 Fitting results of the squared ZTD residuals from 2009 to 2018. Upper left: fitting RMS; upper right: constant term; middle left and right: sine and cosine coefficients of the annual periodical term; lower left and right: sine and cosine coefficients of the semi-annual periodical term. Note the different scales between different panels.

165

The coefficients of annual and semi-annual amplitudes are given in Figure 5. The two amplitudes are calculated as: $amp_{R1} = \sqrt{R_{s1}^2 + R_{c1}^2}$ and $amp_{R2} = \sqrt{R_{s2}^2 + R_{c2}^2}$, and thus the unit is mm². Note that the presented amplitudes do not give the peak-to-peak values of the empirically modeled formal error, and only illustrate the strength of the annual and semi-annual signals. The annual amplitude is rather significant in several regions, such as Northeast China, the middle and western part of Australia, and around the Bay of Bengal (northeastern part of the Indian Ocean). The semi-annual amplitudes are smaller than the annual one, and the distribution generally follows that of the annual one, and large values are observed mainly in the middle and low latitude regions such as the East China Sea between China and Japan, northeast India, and Arabian Sea between India subcontinent and Arabian Peninsula.

170



175

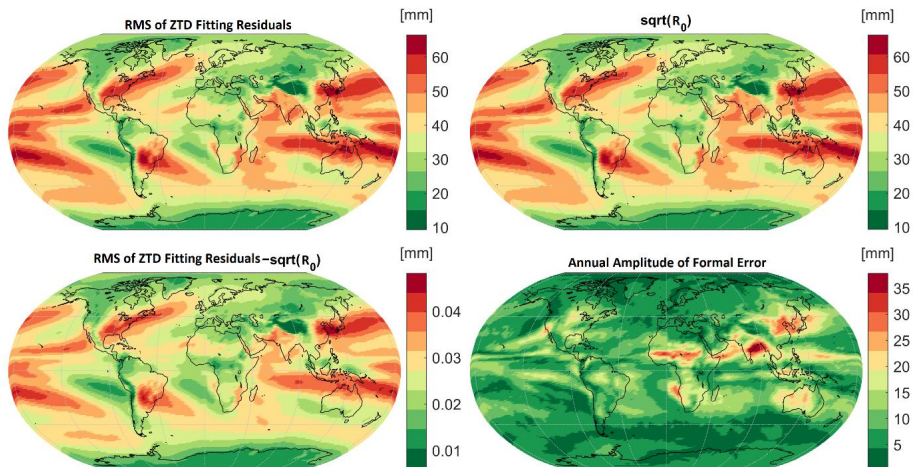
Figure 5 Coefficients of annual (left) and semi-annual (right) amplitude for the ZTD formal error modeling.

In Figure 6, we further compare the RMS values of ZTD modeling residuals (upper left) and the constant term of ZTD formal error (upper right). An excellent agreement is observed as the differences are negligible (lower left panel). The annual amplitude of formal error is also given (lower right panel). The calculation of the annual term does not follow that of the ZTD, as the formal error modeling is based on the squared residuals. Therefore, we simply take half of the peak-to-peak value as the annual amplitude, and do not present the semi-annual amplitude of the formal error. Note that the unit of amplitude is mm.

180



As shown in the lower right panel of Figure 6, the annual amplitude of formal error shows a correlation with the latitude, and that at high latitude regions is below 10 mm. The average amplitude is 6.2 mm on a global scale, and 95% of the grid points are within 16.3 mm. Despite that only a few grid points have large amplitude, the value could still reach up to 30 mm, such as the Northeast China, around the Bay of Bengal (northeastern part of the Indian Ocean), and on the west coast of Africa.



185

Figure 6 Fitting results of the ZTD formal error. Upper left: RMS of ZTD fitting residuals; upper right: average value of formal error; lower left: the difference between RMS of ZTD fitting residuals and average formal error; lower right: amplitude of the sine and cosine coefficients of the annual periodical term. The annual amplitude is calculated as half of the peak-to-peak value.

2.3 Modeling the vertical variation ZTD

190

It is well known that the tropospheric delay has a strong dependence on station altitude due to the altitude dependence of atmospheric pressure (Dousa and Elias, 2014; Wang et al., 2022). Considering that the delays of VMF products refer to a certain altitude of the grid points (shown in Figure 1), users need to apply the height-related correction. Usually, the first-order exponential function can very well describe the vertical lapse of tropospheric delay, especially for the empirical modeling of tropospheric delay which aims at an accuracy of several centimeters. A higher-order exponential function could further improve the vertical modeling precision (Wang et al., 2022), which is not necessary for this work. We adopt the follow equation to account for the correction due to the difference between the altitude of the user h and that of the grid point $h0$.

$$ZTD(h) = ZTD(h0) \cdot \exp\left(-\frac{h-h0}{\beta}\right) \quad (3)$$

β is the scaling height. In this work we use $\beta = 7.6$ km, which is based on the numerical fitting of NWM-derived ZTD from all grid points in 2009–2018.

200

As for the modeling of formal error, it can be easily derived by adopting Eq. (4).

$$\sigma_{ZTD(h)}^2 = \sigma_{ZTD(h0)}^2 \cdot \left(\exp\left(-\frac{h-h0}{\beta}\right) \right)^2 \quad (4)$$

2.4 An empirical ZTD modeling with uncertainty

Eventually, we present the empirical model to provide both zenith delays and the corresponding uncertainty information. The model is based on a $1^\circ \times 1^\circ$ global grid, which has the same altitude as the VMF grid product (https://vmf.geo.tuwien.ac.at/station_coord_files/gridpoint_coord_1x1.txt). At each grid point, five coefficients are used to describe the zenith delay, including one for the constant coefficient, two for the annual and two for the semi-annual terms, as shown in Eq. (1); five coefficients are used to describe the uncertainty, adopting the similar format as the zenith delay. In



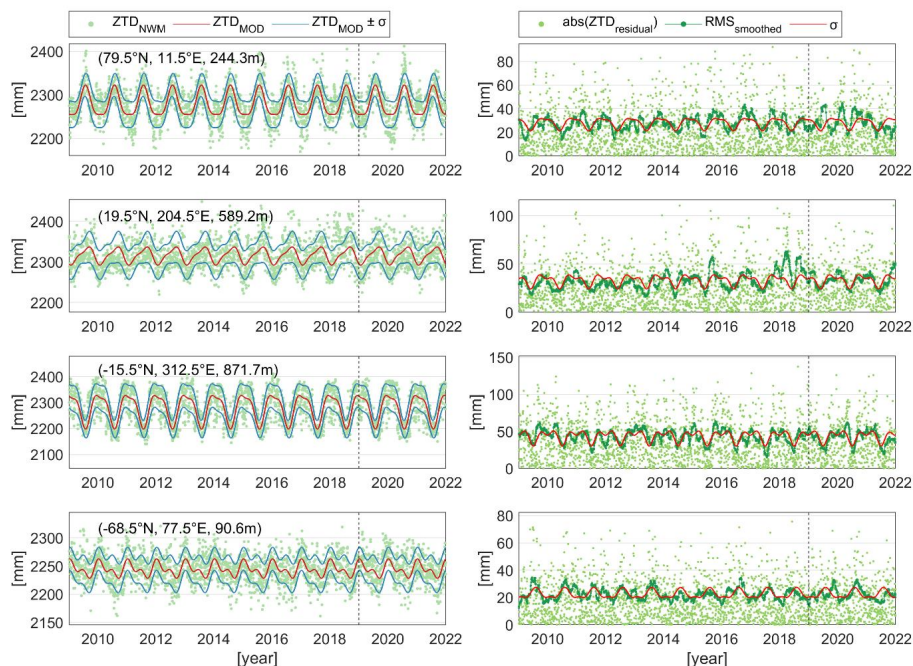
addition, the correction of zenith delay and uncertainty caused by the station height is based on one lapse rate presented in Sect. 2.3.

210 To obtain the zenith delay and uncertainty at a location, the user needs to (a) find four grid points around the user given the latitude and longitude, (b) calculate the zenith delays and uncertainties at these four points using the ten coefficients, (c) apply the altitude corrections for zenith delays and uncertainties with Eq. (3) and Eq. (4) to obtain the values at the user's height, (d) apply the bi-linear interpolation to obtain the values at the user's location.

3 Evaluation with NWM Products

215 First, the performance of the empirically modeled ZTD and formal error is evaluated using NWM-derived ZTD products, that is, the VMF product. Note that the model is established using the data in the period of 2009–2018, and for the evaluation in this section, we focus on the period of 2019–2021. Figure 7 illustrates the time series at four selected grid points in different latitudes, covering different altitudes. The left panels show that the empirically modeled ZTD agrees well with the NWM-derived values, and the majority of the NWM-derived ZTD values are within the uncertainty line. The annual and semi-annual variations of ZTD are also successfully presented by the empirical model. In the right panels, the ZTD modeling residuals and the ZTD formal errors are given. The formal error agrees well with the residuals at the four grid points, and ZTD residuals at the upper two grid points show more significant annual variations than the other two grid points. Moreover, for the periods with larger formal error, that is, the periods where the formal error has a peak value, the ZTD residuals could be extremely 220 large. The reason is that at these periods the water vapor content is more abundant, and extreme weather conditions are also more likely to happen. Therefore, extremely large discrepancies are observed. For both ZTD and the residuals, the agreement between NWM-derived values and empirically modeled ones does not show a significant difference between the modeling period (2009–2018) and the prediction period (2019–2021).

225



230 **Figure 7** Left: ZTD time series (light blue dot) and the empirically modeled values (red line). The formal errors are given in the blue dashed lines. Right: the absolute value of ZTD residuals (green dots), the smoothed RMS of residuals within a period of a 2-month window (green dot-line), and the ZTD modeling formal error (red line). The period for modeling and that for evaluation are



separated by the black dashed line. Note the different vertical scales between different panels. The location of each grid point is given in the left panel.

The statistics of the ZTD modeling error in different seasons of the predicted period, that is, from 2019 to 2021, are provided

235 in the left panels of Figure 7. We also give the corresponding formal errors of ZTD in the right panels. The modeling accuracy shows a clear seasonal dependence, and the error is larger in the Summertime, that is, Jun-Jul-Aug and Dec-Jan-Feb of the North and South Hemispheres, respectively. In the Summertime, the water vapor content is more abundant with more rapid variations which cannot be accurately represented using the empirical model, and thus the modeling errors are relatively large.

The average RMS of all grid points from 2017 to 2021 is 35.3 mm, and the values in Mar-Apr-May, Jun-Jul-Aug, Sep-Oct-

240 Nov, Dec-Jan-Feb are 35.4, 35.0, 35.2, and 35.7 mm, respectively. The formal error shows the same distribution and magnitude as the RMS of ZTD residuals in the four seasons, which demonstrates that the formal error modeling can effectively present the ZTD accuracy with respect to the NWM-derived product. The average value of formal errors in the four seasons is 35.5, 35.1, 35.3, and 35.8 mm, which agrees with the RMS of ZTD residuals at the level of 0.1 mm. We also calculate the differences between the RMS and formal error at each grid point, and the maximum discrepancy is only -0.2 mm, meanwhile, the RMS

245 of the differences over all grid points is less than 0.1 mm.

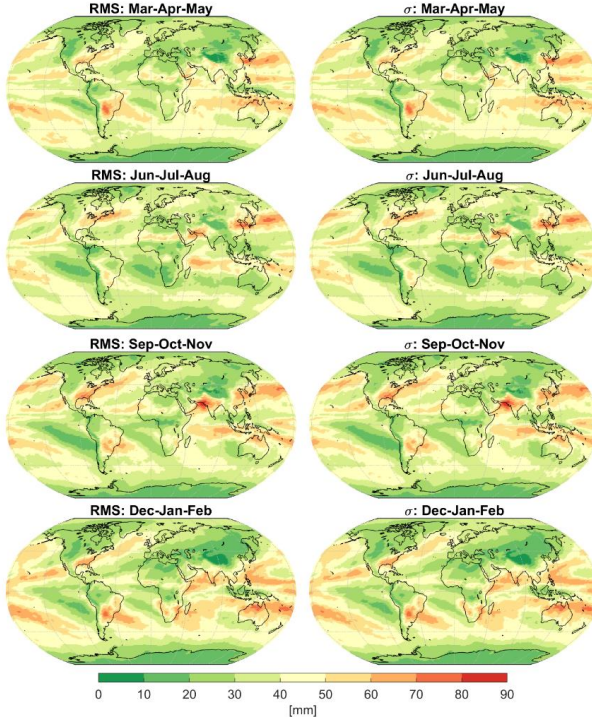


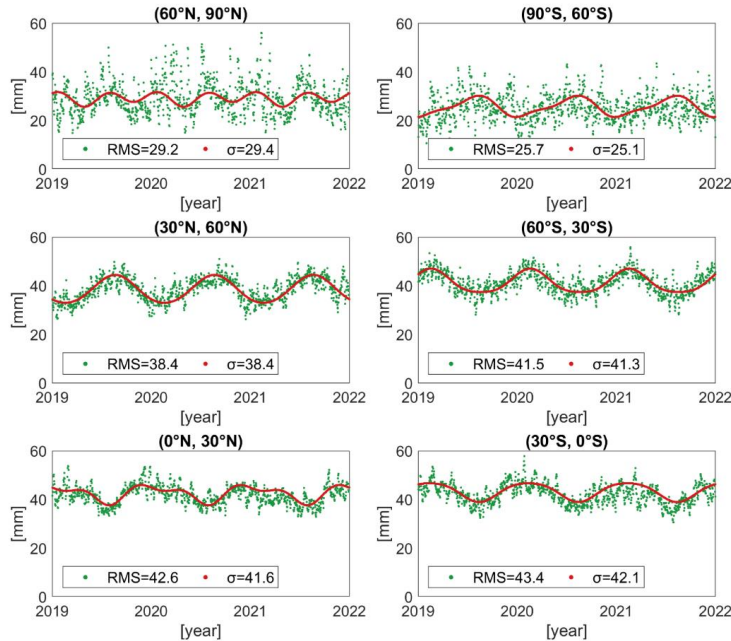
Figure 8 RMS of the ZTD modeling errors (left panels) and the modeling formal errors (right panels) in different seasons from 2018 to 2021.

We further calculate the average values of all grid points within different latitude intervals day by day for both the RMS of

250 ZTD residuals and the formal errors, which are presented in Figure 9. The global grid is divided with a latitude interval of 30°, and on each day we calculate the RMS of ZTD residuals from all grid points and the average formal error. Except for the region of 60°N–90°N where semi-annual signals are also visible, both the RMS of ZTD residuals at other latitudes show significant annual variations, and the formal errors also show a good agreement. The annual variation at the region of 30°N–60°N and 30°S–60°S is larger than that of the other regions, which is mainly caused by the large amplitude of the annual term in modeling formal error in several locations such as north-east Asia, middle-west Australia (also shown in Figure 6). Moreover,



the RMS values of ZTD residuals are smaller at higher latitudes than at lower latitudes, as the latter has more water vapor content which is more difficult to model empirically. However, the Pole regions (latitude higher than 60°), especially the north one, show larger temporal noises than other regions.



260 **Figure 9 RMS of ZTD differences between the empirical model and the NWM-derived values, averaged value of all grid points in different latitude intervals (green dot), and the corresponding ZTD formal errors (red dot). On each day, the average value of all the grid points within the latitude range is presented.**

4 Evaluation with GNSS ZTD products

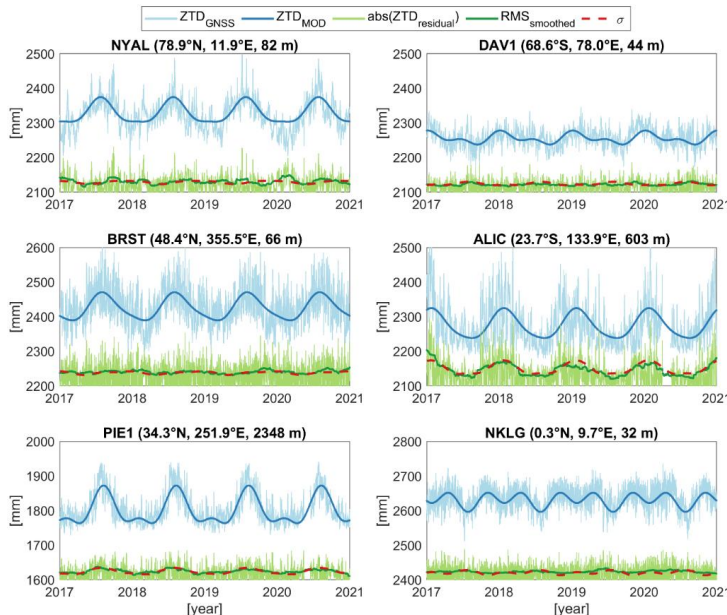
In this section, we evaluate the empirical ZTD model using ZTD estimates from GNSS observations. We select 380 IGS stations that have good coverage from 2017 to 2020 (shown in Figure 1) and use the ZTD estimates from the Nevada Geodetic Laboratory (NGL) product (Blewitt et al., 2018). The NGL tropospheric products are processed with the PPP method using the GipsyX software. The repro3 final orbit and clock products from the JPL analysis center are fixed. For tropospheric delay modeling, a priori delays and mapping functions are derived from the VMF1 product. The residual ZWD and horizontal gradients are estimated using the random walk processes with a temporal resolution of 5 min, and the corresponding stochastic noise is 5.d-8 and 5.d-9 km/sqrt(sec). More details can be found in the data processing strategy description file (<http://geodesy.unr.edu/gps/ngl.acn.txt>). The NGL tropospheric delay products are widely used in tropospheric delay empirical modeling, model evaluation, and comparison with NWM-derived products (Chen et al., 2020; Ding et al., 2022; Pearson et al., 2020; Yu et al., 2021; Yuan et al., 2022). We selected the period of 2017 to 2020 because the modeling is based on the NWM-derived product in the period of 2009 to 2018, and thus the period of 2019 and 2020 is always predicted.

275 We first use six IGS stations as an example to present the ZTD modeling accuracy, which covers different latitudes and altitudes. Figure 10 gives the ZTD estimates from GNSS and from the empirical model (in light and dark blue lines, respectively). In general, the empirical model can effectively capture the long-term variation of ZTD, mostly the annual and semi-annual signals. However, the short-term fluctuations cannot be modeled empirically, leaving large residuals up to tens of centimeters, especially in the summertime. The residuals at BRST are larger and that at DAV1 is smaller, mainly because BRST is located on the coast of France with high water vapor content and DAV1 is located in the Antarctic with lower water vapor content. Note that the ZTD at PIE1 is smaller than that at other stations, due to the higher station altitude.



285

To inspect the modeling performance of formal error, we give the absolute values of the ZTD residuals (in light green line), that is, the GNSS estimates minus the empirical modeled values. Depending on the location, ZTD residuals show different variations. For instance, at ALIC (central Australia) the residuals show clear annual variations of several centimeters, which is consistent with the modeled amplitude of the formal error in Figure 6. The station PIE1 (Pie Town, southwest U.S.A.) also shows annual variations but the magnitude is much smaller, and the other four stations have no significant annual signals. We further compare the modeled formal error (“ σ ” in red dashed line) and the smoothed RMS of ZTD residuals (“RMS_{smoothed}” in dark green line), that is, one RMS of the residuals within a period of 2 months. The two values are overlapped to a large extent, meaning that the modeled formal error agrees well with the residuals.



290

Figure 10 ZTD estimates from GNSS (“ZTD_{GNSS}”) and empirical model (“ZTD_{MOD}”), and the corresponding residuals (“abs(ZTD_{residual})”). The smoothed RMS of ZTD residuals within a 2-month window (“RMS_{smoothed}”) and the formal error of the empirical model (“ σ ”) are also given. Note that the absolute values of ZTD residuals are given. ZTD residuals, the RMS values, and the formal errors are shifted with the same bias for better visibility. The GNSS station name and location are given in the title of each panel.

295

300

The RMS of ZTD residuals within a 2-month period and the formal error at more GNSS stations are presented in Figure 11. We select one station every 5° in latitude, and in total 32 GNSS stations are given. As shown, the formal error has a very good agreement with the RMS of residuals at most of the stations. For stations with a small magnitude of formal error, the fluctuation of residual RMS also tends to be a straight line with some noises instead of showing any annual variations, and for stations with significant annual signals, the formal error also shows a very similar pattern. Despite the generally good agreement between the RMS of ZTD residuals and formal error, it is worth mentioning that the short-term noises still exist, for instance, at station MRO1 (27°S) the RMS is about 30 mm larger than the formal error at the beginning period of the year 2017, and at station KIRI (1°N) the RMS value could be 20 mm smaller than the formal error in 2017. This is expected as the RMS values present the real accuracy of the empirical model whereas the formal error can only provide the average value and annual variation based on long-term numerical fitting. The semi-annual periodical signals are also significantly visible at several stations, such as BRMU (32°N), HYDE (17°N), MRO1 (27°S), and DGAR (7°S).

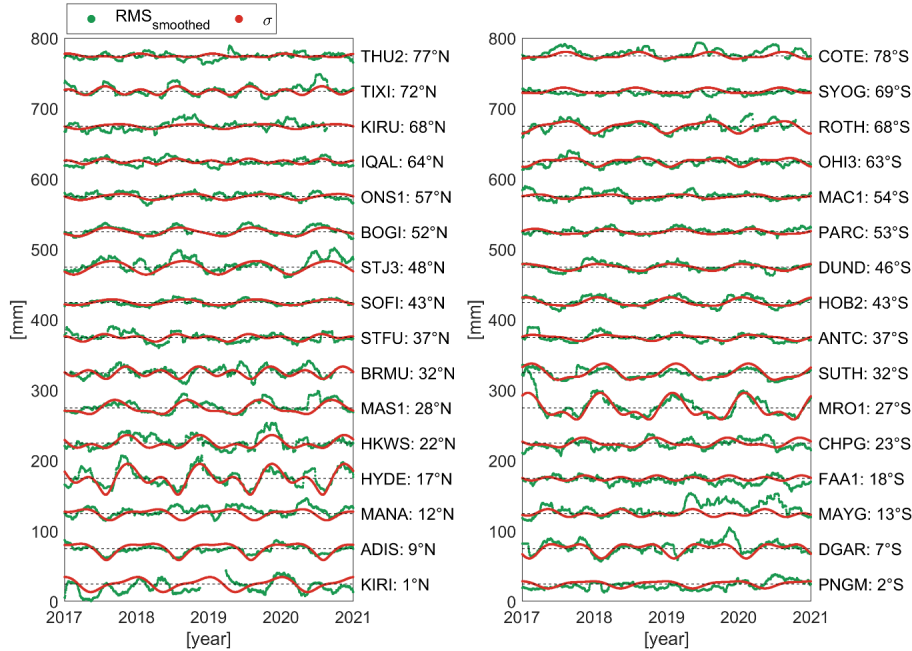


Figure 11 Smoothed RMS of ZTD modeling residuals using a 2-month window (green dots) and the formal errors (red dots) at selected GNSS stations. Stations in the North and South Hemispheres are given in left and right panels, respectively, sorted by latitude. The time series are shifted for better visibility.

310

The agreement between the RMS of ZTD residuals and the formal errors is further analyzed in Figure 12. As shown in the left panel, the agreement is rather optimal and a strong correlation is observed. The correlation coefficient is 96%, meaning that the formal error can effectively present the accuracy of the empirical ZTD model over the four years, that is, 2017 to 2020. Both the overall RMS of the whole period (“RMS_{all}”) and the average value of the smoothed RMS time series over the 2-month periods show good agreement with the formal error. Taking all stations into consideration, the average bias of residual ZTD is -0.4 mm, the mean RMS of ZTD residuals is 38 mm, and the mean value of formal errors is 36 mm.

315

We also give the correlation coefficients between the smoothed RMS of ZTD residuals within a 2-month period and the corresponding formal error in the right panel. For most stations, the correlation coefficients are quite large, especially for those with a large annual amplitude of formal error. The number of stations with a magnitude larger than 20 mm and between 10 and 20 mm is 29 and 103, respectively, and the corresponding average correlation coefficient is 85% and 77%. The average value of all correlation coefficients, including those with a negative value, is 63%, and the median one is 70%. For stations with a small annual magnitude of formal error, the correlation coefficient is small or even negative. A small magnitude means that the formal error tends to be a straight line, for example, station THU2 (77°N), IQAL (64°N), and MAC1 (54°S) in Figure 11, and thus any discrepancy between the RMS of residuals and formal error caused by the noise of the RMS could degrade the correlation coefficient.

320

325

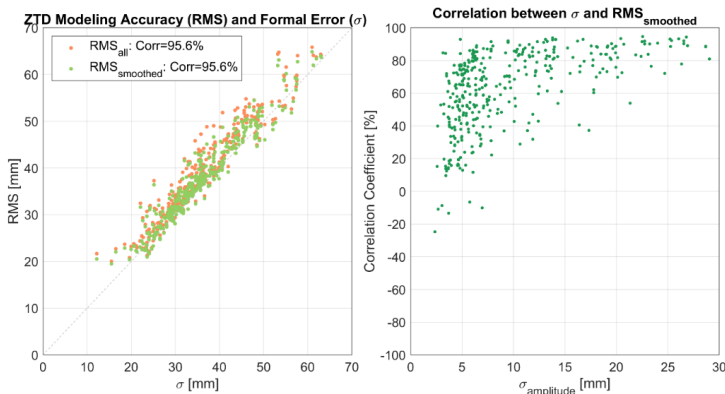


Figure 12 Left: ZTD modeling accuracy (vertical axis) and formal error (horizontal axis) at GNSS stations from 2017 to 2020. For each GNSS station, the RMS of all ZTD modeling residuals in 2017–2020 is given in the yellow dots (“RMS_{all}”), and the average value of all RMS values in each 2-month window is given in the green dots (“RMS_{smoothed}”). Right: correlation coefficients between the ZTD formal error and RMS of a 2-month time window as a function of the formal error annual amplitude. The correlation coefficients in the right panel are all statistically significant with the p-value smaller than 0.05.

330

5 Impact on the convergence time of kinematic PPP solution

335

To evaluate the impact of using the empirical ZTD model and the corresponding uncertainty information on GNSS positioning, we conduct a pseudo-kinematic PPP solution using the 200 globally distributed IGS stations (shown in Figure 1). The 30-sec sampled GPS observations in DOY 001–030, 091–120, 180–210, and 271–300, which correspond to the four seasons, are processed. Each day, we cut the 24-hour data into six arcs, and process only four hours of data per solution. In total around 720 solutions are processed for each station, depending on the availability of observations.

340

The Positioning And Navigation Data Analyst (PANDA) software (Liu & Ge, 2003; Geng et al., 2008) with multi-technique processing developments (Wang et al., 2022) are used for the data processing. We adopt the conventions in the IGS third reprocessing campaign (Repro3, <http://acc.igs.org/repro3/repro3.html>) for the pseudo-kinematic PPP solutions, where the satellite orbits and clocks are fixed to ESA’s Repro3 products. For parameter estimation, we estimate ambiguity as constant per arc, epoch-wise station coordinates, receiver clocks, and zenith tropospheric delays mapped by the VMF3. The tropospheric gradients are not estimated as they are not critical for the kinematic PPP accuracy but degrade the convergence speed (Wang & Liu, 2019; Cui et al., 2022). A stochastic processing noise of 5 mm/sqrt(h) is applied to the epoch-wise ZTD estimates. The a priori ZHD is provided by the VMF3 products, and the a priori ZWD is provided by our empirical ZTD model, that is, the empirical ZTD minus the ZHD from VMF3. Note that it is also possible to adopt other empirical ZHD models, such as the GPT series. The ZWD estimates are constrained to the a priori delay with different weights: 1 m considered as a very loose constraint (solution “No”), one and two times the uncertainty from our empirical model (solution “1 σ ” and “2 σ ”, respectively). We evaluate both 5° and 15° cut-off elevation angles, which represent an ideal and a normal case, respectively. The positioning results are evaluated by comparing them with the IGS Repro3 combined coordinates.

345

Figure 13 presents the RMS value of positioning errors in the first two hours of each solution. Note that we calculate the average RMS with a time window of 10-min. In general, applying a proper constraint to the a priori tropospheric delay can improve the positioning performance in the convergence period, that is, speeding up the convergence time, especially in the first 30 minutes. For the 15° cut-off elevation angle solutions, both 1 σ and 2 σ constraints improve the convergence speed, and the improvement of the first case is less significant after 40 minutes. As for the 5° cut-off elevation angle solutions, the 1 σ and 2 σ constraints improve the convergence speed with respect to the loose-constrained solution in the first 20 minutes, whereas after that, only the 2 σ solution is improved and the 1 σ one gets degraded. The positioning results are combined contributions of both real GNSS observations and the axillary information, that is, the external tropospheric delays and the corresponding

350

355



uncertainties in this case. When the contribution of GNSS observation is less robust, for example, at the beginning of a session, especially with a higher cut-off elevation angle, the observation geometry is not good enough to provide good estimates, and thus introducing external tropospheric delays and uncertainties contributes to stabilizing the solution and improving the convergence. When a good observation geometry is available, that is, after the convergence time or with more satellites available, GNSS observation itself can provide robust and accurate coordinates, and the additional tropospheric delay information does not contribute significantly. On the other hand, if a tight constraint is applied, the tropospheric delay error propagates into the coordinates and degrades the solution accuracy.

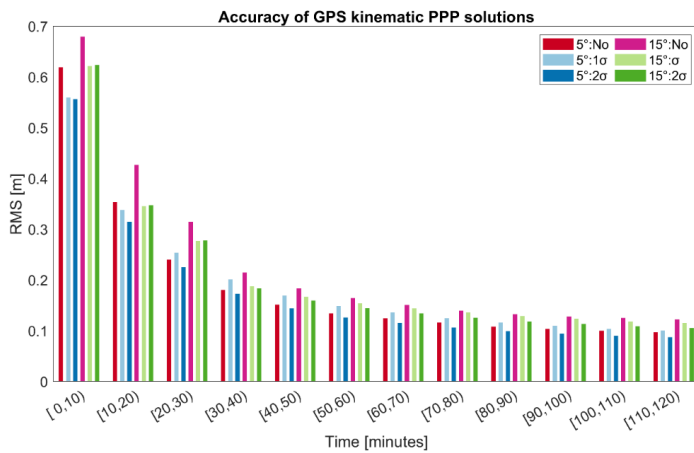


Figure 14 Positioning accuracy of pseudo-kinematic GPS PPP solutions with different constraints on tropospheric delays under different cut-off elevation angles. The RMS value in the first two hours of each solution over a 10-min time window is presented.

6 Conclusions and Outlook

Empirical tropospheric delay models are important for real-time GNSS applications as they provide precise a priori zenith delays with an accuracy of 3 to 4 cm and are easy to implement without any external meteorological input. They serve as both a priori delays and constraints to accelerate the convergence time, and in the latter case, uncertainty is required. Currently, most empirical delay models, such as the GPT series, provide only the delay values but not the uncertainty information. As a consequence, the users have to numerically test the impact of different values (Yao et al., 2017), which has a dependence on both the location and season.

We present a global model to provide both zenith tropospheric delays and the corresponding uncertainties, which facilitates exploiting empirical delay models in enhancing real-time GNSS applications. Based on ten years (2009–2018) of NWM-derived zenith delay grids with a spatial resolution of $1^\circ \times 1^\circ$, we derive the numerically fitted coefficients, which can present ZTD with an accuracy of 36 mm on a global scale. After obtaining the fitting residuals of the delays, we further model the squared residuals using a function containing constant, annual, and semi-annual terms, which present the average value and seasonal variations of the uncertainty (formal error). The constant term of formal error varies between 10 and 60 mm at different locations, and the annual amplitude could reach up to 30 mm and the global average value is 6.2 mm. Eventually, we provide a $1^\circ \times 1^\circ$ global grid, and at each grid point, five coefficients are used to present ZTD and five for formal error.

To evaluate the proposed model, we use both NWM-derived delays in 2019–2021 and ZTD estimates from 380 GNSS stations in 2017–2020. The comparison with NWM-derived ZTD values shows that the model accuracy is around 35 mm, and the seasonal variations of the ZTD formal error agree with the ZTD accuracy within 0.1 mm on average. The agreement of our empirical ZTD model with GNSS ZTD estimates is 38 mm in terms of the RMS statistic, and the average bias is 0.4 mm. The modeled ZTD formal error has a strong correlation with the ZTD accuracy and the correlation coefficient is 96%. Inspecting



the seasonal variations of the formal error, the stations with a larger annual amplitude of formal error have larger correlation
390 coefficients. For example, for stations with an amplitude larger than 20 mm, the average correlation is 84%.

Note that our empirical model does not aim for a higher modeling accuracy. Instead, we provide the additional uncertainty
information of the delay values to users. On the one hand, the empirical modeling accuracy of zenith tropospheric delay is
limited to 3 to 4 cm with the commonly used strategies. This can be easily verified by the numerical fitting of ZTD from NWM
and/or GNSS. Given the NWM-derived ZTD time series, the numerical fitting accuracy of the typical method, that is, annual
395 and semi-annual periodical terms, is around 36 mm (for example, in Figure 2). Considering that the ZTD agreement between
NWM and GNSS estimates are around 1 to 1.5 cm (Zhou et al., 2020), the fitting accuracy of GNSS ZTD is expected to be at
the same level (also see Chen et al. (2020)). In any case, to achieve better accuracy for the tropospheric delay empirical
modeling, more sophisticated methods should be used in the future, such as machine learning and artificial intelligence, which
are already utilized in the regional tropospheric delay augmentation and water vapor sensing (Miotti et al., 2020; Shehaj et al.,
400 2022; Zhang et al., 2022; Zheng et al., 2022). On the other hand, the uncertainty information is beneficial to real-time GNSS
users, especially in the scenarios of enhancing the convergence speed. As the uncertainty shows large differences between
different locations and seasons, it is not optimal to use arbitrary values, and our proposed model can thus provide a realistic
reference. As the uncertainty modeling is based on a similar dataset as the GPT series, it is also applicable to the GPT series.
Therefore, the modeled uncertainty information is also useful for GNSS integrity monitoring, where bounding the residual
405 tropospheric delay is beneficial for the vertical alert limits (Lai et al., 2023; McGraw G, 2012; Rózsa et al., 2020; Su & Schön,
2022; Yang et al., 2023). For future study, it would also be possible to provide the mapping function modeling error for the
empirical mapping functions such as GPT3/VMF3, whereas how to utilize the uncertainty of mapping functions still needs
investigation.

Code Availability

410 The model referred to as SHAtrop_Sigma is provided at <https://zenodo.org/records/11563994> (doi: 10.5281/zenodo.11563993)
and also available at the GNSS Analysis Center at Shanghai Astronomical Observatory:
http://center.shao.ac.cn/shao_gnss_ac//index.html.

Data Availability

The tropospheric delay product from NWM is available at <http://doi.org/10.17616/R3RD2H>, the GNSS ZTD estimates are
415 available at: http://geodesy.unr.edu/gps_timeseries/trop/.

Author Contributions

All authors contributed to the study's conception and design. Material preparation, data collection, and analysis were performed
by Jungang Wang and Junping Chen. The first draft of the manuscript was written by Jungang Wang and all authors commented
on previous versions of the manuscript. All authors read and approved the final manuscript.

420 Competing interests

The authors declare that they have no conflicts of interest.



Acknowledgments

We would like to thank TU Wien for providing the tropospheric delay products (<http://doi.org/10.17616/R3RD2H>), and NGL for providing the GNSS ZTD (<http://geodesy.unr.edu/>). Jungang Wang is funded by the Helmholtz OCPC Program (grant no. 425 ZD202121) and the DFG COCAT Project (Nr. 490990195). Junping Chen is supported by the Program of Shanghai Academic/Technology Research Leader (No. 20XD1401500).

References

Alber, C., R. Ware, C. Rocken, and F. Solheim (1997), GPS surveying with 1 mm precision using corrections for atmospheric slant path delay, *Geophysical Research Letters*, 24(15), 1859-1862, doi:10.1029/97gl01877.

430 Askne, J., and H. Nordius (1987), Estimation of tropospheric delay for microwaves from surface weather data, *Radio Science*, 22(3), 379-386, doi:10.1029/RS022i003p00379.

Böhm, J., R. Heinkelmann, and H. Schuh (2007), Short Note: A global model of pressure and temperature for geodetic applications, *Journal of Geodesy*, 81, 678-683, doi:10.1007/s00190-007-0135-3.

435 Böhm, J., G. Möller, M. Schindelegger, G. Pain, and R. Weber (2015), Development of an improved empirical model for slant delays in the troposphere (GPT2w), *GPS Solutions*, 19(3), 433-441, doi:10.1007/s10291-014-0403-7.

Böhm, J., A. Niell, P. Tregoning, and H. Schuh (2006), Global Mapping Function (GMF): A new empirical mapping function based on numerical weather model data, *Geophysical Research Letters*, 33(7), doi:10.1029/2005gl025546.

440 Böhm, J., and H. Schuh (2013), *Atmospheric Effects in Space Geodesy*, XVII, 234 pp., Springer-Verlag Berlin Heidelberg, doi:10.1007/978-3-642-36932-2.

Blewitt, G., W. Hammond, and C. Kreemer (2018), Harnessing the GPS Data Explosion for Interdisciplinary Science, *Eos*, 99, doi:10.1029/2018eo104623.

Bock, O., J. Tarniewicz, C. Thom, J. Pelon, and M. Kasser (2001), Study of external path delay correction techniques for high accuracy height determination with GPS, *Physics and Chemistry of the Earth, Part A: Solid Earth and Geodesy*, 26(3), 165-171, doi:10.1016/s1464-1895(01)00041-2.

445 Bosser, P., O. Bock, C. Thom, J. Pelon, and P. Willis (2009), A case study of using Raman lidar measurements in high-accuracy GPS applications, *Journal of Geodesy*, 84(4), 251-265, doi:10.1007/s00190-009-0362-x.

Braun, J., C. Rocken, and J. Liljegren (2003), Comparisons of Line-of-Sight Water Vapor Observations Using the Global Positioning System and a Pointing Microwave Radiometer, *Journal of Atmospheric and Oceanic Technology*, 20(5), 606-612, doi:10.1175/1520-0426(2003)20<606:colosw>2.0.co;2.

450 Chen, B., and Z. Liu (2016), Global water vapor variability and trend from the latest 36 year (1979 to 2014) data of ECMWF and NCEP reanalyses, radiosonde, GPS, and microwave satellite, *Journal of Geophysical Research: Atmospheres*, 121(19), 11,442-11,462, doi:10.1002/2016jd024917.

Chen, J., J. Wang, A. Wang, J. Ding, and Y. Zhang (2020), SHAtropE—A Regional Gridded ZTD Model for China and the Surrounding Areas, *Remote Sensing*, 12(1), 165, doi:10.3390/rs12010165.

455 Cui, B., J. Wang, P. Li, M. Ge, and H. Schuh (2022), Modeling wide-area tropospheric delay corrections for fast PPP ambiguity resolution, *GPS Solutions*, 26(2), doi:10.1007/s10291-022-01243-1.

de Oliveira, P. S., L. Morel, F. Fund, R. Legros, J. F. G. Monico, S. Durand, and F. Durand (2016), Modeling tropospheric wet delays with dense and sparse network configurations for PPP-RTK, *GPS Solutions*, 21(1), 237-250, doi:10.1007/s10291-016-0518-0.

460 Ding, J., and J. Chen (2020), Assessment of Empirical Troposphere Model GPT3 Based on NGL's Global Troposphere Products, *Sensors (Basel)*, 20(13), doi:10.3390/s20133631.



Ding, J., J. Chen, W. Tang, and Z. Song (2022), Spatial–Temporal Variability of Global GNSS-Derived Precipitable Water Vapor (1994–2020) and Climate Implications, *Remote Sensing*, 14(14), 3493, doi:10.3390/rs14143493.

Dousa, J., and M. Elias (2014), An improved model for calculating tropospheric wet delay, *Geophysical Research Letters*, 41(12), 4389-4397, doi:10.1002/2014gl060271.

Douša, J., M. Eliaš, P. Václavovic, K. Eben, and P. Krč (2018), A two-stage tropospheric correction model combining data from GNSS and numerical weather model, *GPS Solutions*, 22(3), doi:10.1007/s10291-018-0742-x.

Geng, J., Shi, C., Zhao, Q., Ge, M., Liu, J. (2008). Integrated Adjustment of LEO and GPS in Precision Orbit Determination. In: Xu, P., Liu, J., Dermanis, A. (eds) VI Hotine-Marussi Symposium on Theoretical and Computational Geodesy. International Association of Geodesy Symposia, vol 132. Springer, Berlin, Heidelberg. https://doi.org/10.1007/978-3-540-74584-6_20

Hopfield, H. S. (1969), Two-quartic tropospheric refractivity profile for correcting satellite data, *Journal of Geophysical Research*, 74(18), 4487-4499, doi:10.1029/JC074i018p04487.

Hu, Y., Yao, Y. A new method for vertical stratification of zenith tropospheric delay. *Adv. Space Res.* (2018), <https://doi.org/10.1016/j.asr.2018.10.035>

Huang, L., G. Zhu, L. Liu, H. Chen, and W. Jiang (2021), A global grid model for the correction of the vertical zenith total delay based on a sliding window algorithm, *GPS Solutions*, 25(3), doi:10.1007/s10291-021-01138-7.

Huang, L., G. Zhu, H. Peng, L. Liu, C. Ren, and W. Jiang (2022), An improved global grid model for calibrating zenith tropospheric delay for GNSS applications, *GPS Solutions*, 27(1), doi:10.1007/s10291-022-01354-9.

Kos, T., M. Botincan, and I. Markezic (2009), Evaluation of EGNOS Tropospheric Delay Model in South-Eastern Europe, *Journal of Navigation*, 62(2), 341-349, doi:10.1017/s0373463308005146.

Kouba, J. (2007), Implementation and testing of the gridded Vienna Mapping Function 1 (VMF1), *Journal of Geodesy*, 82(4-5), 193-205, doi:10.1007/s00190-007-0170-0.

Kouba, J. (2009), Testing of global pressure/temperature (GPT) model and global mapping function (GMF) in GPS analyses, *Journal of Geodesy*, 83(3-4), 199-208, doi:10.1007/s00190-008-0229-6.

Lagler, K., M. Schindelegger, J. Bohm, H. Krasna, and T. Nilsson (2013), GPT2: Empirical slant delay model for radio space geodetic techniques, *Geophys Res Lett*, 40(6), 1069-1073, doi:10.1002/grl.50288.

Lai, Yu-Fang, Blanch, Juan, Walter, Todd, Troposphere Delay Model Error Analysis With Application to Vertical Protection Level Calculation. Proceedings of the 2023 International Technical Meeting of The Institute of Navigation, Long Beach, California, January 2023, pp. 903-921. <https://doi.org/10.33012/2023.18615>

Landskron, D., and J. Böhm (2017), VMF3/GPT3: refined discrete and empirical troposphere mapping functions, *Journal of Geodesy*, 92(4), 349-360, doi:10.1007/s00190-017-1066-2.

Leandro, R. F., R. B. Langley, and M. C. Santos (2007), UNB3m_pack: a neutral atmosphere delay package for radiometric space techniques, *GPS Solutions*, 12(1), 65-70, doi:10.1007/s10291-007-0077-5.

Li, T., L. Wang, R. Chen, W. Fu, B. Xu, P. Jiang, J. Liu, H. Zhou, and Y. Han (2021), Refining the empirical global pressure and temperature model with the ERA5 reanalysis and radiosonde data, *Journal of Geodesy*, 95(3), doi:10.1007/s00190-021-01478-9.

Li, W., Y. Yuan, J. Ou, Y. Chai, Z. Li, Y.-A. Liou, and N. Wang (2014), New versions of the BDS/GNSS zenith tropospheric delay model IGGtrop, *Journal of Geodesy*, 89(1), 73-80, doi:10.1007/s00190-014-0761-5.

Li, W., Y. Yuan, J. Ou, and Y. He (2018), IGGtrop_SH and IGGtrop_rH: Two Improved Empirical Tropospheric Delay Models Based on Vertical Reduction Functions, *IEEE Transactions on Geoscience and Remote Sensing*, 56(9), 5276-5288, doi:10.1109/tgrs.2018.2812850.

Li, W., Y. Yuan, J. Ou, H. Li, and Z. Li (2012), A new global zenith tropospheric delay model IGGtrop for GNSS applications, *Chinese Science Bulletin*, 57(17), 2132-2139, doi:10.1007/s11434-012-5010-9.



505 Liou, Y. A., Y. T. Teng, T. V. Hove, and J. C. Liljegren (2001), Comparison of precipitable water observations in the near tropics by GPS, microwave radiometer, and radiosondes, *J. Appl. Meteor.*, 40, 5-15.

510 Lu, C., X. Li, F. Zus, R. Heinkelmann, G. Dick, M. Ge, J. Wickert, and H. Schuh (2017), Improving BeiDou real-time precise point positioning with numerical weather models, *Journal of Geodesy*, 91(9), 1019-1029, doi:10.1007/s00190-017-1005-2.

515 Mao, J., Q. Wang, Y. Liang, and T. Cui (2021), A new simplified zenith tropospheric delay model for real-time GNSS applications, *GPS Solutions*, 25(2), doi:10.1007/s10291-021-01092-4.

520 McGraw G (2012) Tropospheric error modeling for high integrity airborne GNSS navigation. In: Proc. IEEE/ION PLANS 2012, Institute of Navigation, Myrtle Beach, South Carolina, USA, April 24–26, 158–166.

525 Miotti, L., E. Shehaj, A. Geiger, S. D'Aronco, J. D. Wegner, G. Moeller, and M. Rothacher (2020), Tropospheric delays derived from ground meteorological parameters: comparison between machine learning and empirical model approaches, 1-10, doi:10.23919/enc48637.2020.9317442.

Niell, A. E., A. J. Coster, F. S. Solheim, V. B. Mendes, P. C. Toor, R. B. Langley, and C. A. Upham (2001), Comparison of Measurements of Atmospheric Wet Delay by Radiosonde, Water Vapor Radiometer, GPS, and VLBI, *Journal of Atmospheric and Oceanic Technology*, 18(6), 830-850, doi:10.1175/1520-0426(2001)018<0830:comoaw>2.0.co;2.

530 Pearson, C., P. Moore, and S. Edwards (2020), GNSS assessment of sentinel-3A ECMWF tropospheric delays over inland waters, *Advances in Space Research*, 66(12), 2827-2843, doi:10.1016/j.asr.2020.07.033.

Penna, N., A. Dodson, and W. Chen (2001), Assessment of EGNOS tropospheric correction model, *Journal of Navigation*, 54(1), 37-55, doi:10.1017/S0373463300001107.

Rózsa, S., Ambrus, B., Juni, I. et al. An advanced residual error model for tropospheric delay estimation. *GPS Solut* 24, 103 (2020). <https://doi.org/10.1007/s10291-020-01017-7>

535 Saastamoinen, J. (1972), Atmospheric Correction for the Troposphere and Stratosphere in Radio Ranging Satellites, In: *The Use of Artificial Satellites for Geodesy* (eds S. W. Henriksen, A. Mancini and B. H. Chovitz). 247-251, doi:10.1029/GM015P0247.

Schüler, T. (2013), The TropGrid2 standard tropospheric correction model, *GPS Solutions*, 18(1), 123-131, doi:10.1007/s10291-013-0316-x.

540 Shehaj, E., L. Miotti, A. Geiger, S. D'Aronco, J. D. Wegner, G. Moeller, B. Soja, and M. Rothacher (2022), High-resolution tropospheric refractivity fields by combining machine learning and collocation methods to correct earth observation data, *Acta Astronautica*, doi:10.1016/j.actaastro.2022.10.007.

Su, J., Schön, S. (2022). Bounding the Residual Tropospheric Error by Interval Analysis. In: International Association of Geodesy Symposia. Springer, Berlin, Heidelberg. https://doi.org/10.1007/1345_2022_184

545 Sun, Z., B. Zhang, and Y. Yao (2019), An ERA5-Based Model for Estimating Tropospheric Delay and Weighted Mean Temperature Over China With Improved Spatiotemporal Resolutions, *Earth and Space Science*, 6(10), 1926-1941, doi:10.1029/2019ea000701.

Takeichi, N., T. Sakai, S. Fukushima, and K. Ito (2009), Tropospheric delay correction with dense GPS network in L1-SAIF augmentation, *GPS Solutions*, 14(2), 185-192, doi:10.1007/s10291-009-0133-4.

Wang, J., K. Balidakis, F. Zus, X. Chang, M. Ge, R. Heinkelmann, and H. Schuh (2022), Improving the Vertical Modeling of Tropospheric Delay, *Geophysical Research Letters*, 49(5), doi:10.1029/2021gl096732.

Wang, J., Ge, M., Glaser, S. et al. Improving VLBI analysis by tropospheric ties in GNSS and VLBI integrated processing. *J Geod* 96, 32 (2022). <https://doi.org/10.1007/s00190-022-01615-y>

550 Wang, J., and Z. Liu (2019), Improving GNSS PPP accuracy through WVR PWV augmentation, *Journal of Geodesy*, 93(9), 1685-1705, doi:10.1007/s00190-019-01278-2.



Wang, X.; Zhu, G.; Huang, L.; Wang, H.; Yang, Y.; Li, J.; Huang, L.; Zhou, L.; Liu, L. Development of a ZTD Vertical Profile Model Considering the Spatiotemporal Variation of Height Scale Factor with Different Reanalysis Products in China. *Atmosphere* 2022, 13, 1469. <https://doi.org/10.3390/atmos13091469>

Ware, R., C. Rocken, F. Solheim, T. Van Hove, C. Alber, and J. Johnson (1993), Pointed water vapor radiometer corrections for accurate global positioning system surveying, *Geophysical Research Letters*, 20(23), 2635-2638, doi:10.1029/93gl02936.

Wilgan, K., T. Hadas, P. Hordyniec, and J. Bosy (2017), Real-time precise point positioning augmented with high-resolution numerical weather prediction model, *GPS Solutions*, 21(3), 1341-1353, doi:10.1007/s10291-017-0617-6.

Wu, Z. L., J. G. Wang, Y. X. Liu, X. F. He, Y. Liu, and W. X. Xu (2019), Validation of 7 Years in-Flight HY-2A Calibration Microwave Radiometer Products Using Numerical Weather Model and Radiosondes, *Remote Sensing*, 11(13), 1616, doi:ARTN 1616

555 10.3390/rs11131616.

Xu, C., Y. Yao, J. Shi, Q. Zhang, and W. Peng (2020), Development of Global Tropospheric Empirical Correction Model with High Temporal Resolution, *Remote Sensing*, 12(4), 721, doi:10.3390/rs12040721.

Yang, L., Fu, Y., Zhu, J. et al. Overbounding residual zenith tropospheric delays to enhance GNSS integrity monitoring. *GPS Solut* 27, 76 (2023). <https://doi.org/10.1007/s10291-023-01408-6>

560 Yao, Y., Y. Hu, C. Yu, B. Zhang, and J. Guo (2016), An improved global zenith tropospheric delay model GZTD2 considering diurnal variations, *Nonlinear Processes in Geophysics*, 23(3), 127-136, doi:10.5194/npg-23-127-2016.

Yao, Y., W. Peng, C. Xu, and S. Cheng (2017), Enhancing real-time precise point positioning with zenith troposphere delay products and the determination of corresponding tropospheric stochastic models, *Geophysical Journal International*, 208(2), 565 1217-1230, doi:10.1093/gji/ggw451.

Yao, Y., C. Xu, J. Shi, N. Cao, B. Zhang, and J. Yang (2015), ITG: A New Global GNSS Tropospheric Correction Model, *Sci Rep*, 5, 10273, doi:10.1038/srep10273.

Yao, Y., C. Yu, and Y. Hu (2014), A New Method to Accelerate PPP Convergence Time by using a Global Zenith Troposphere Delay Estimate Model, *Journal of Navigation*, 67(05), 899-910, doi:10.1017/s0373463314000265.

570 Yu, C., Z. Li, and G. Blewitt (2021), Global Comparisons of ERA5 and the Operational HRES Tropospheric Delay and Water Vapor Products With GPS and MODIS, *Earth and Space Science*, 8(5), doi:10.1029/2020ea001417.

Yuan, P., et al. (2022), An enhanced integrated water vapour dataset from more than 10,000 global ground-based GPS stations in 2020, *Earth Syst. Sci. Data Discuss*, doi:10.5194/essd-2022-274.

Zhang, H., Y. Yuan, and W. Li (2022), Real-time wide-area precise tropospheric corrections (WAPTCs) jointly using GNSS and NWP forecasts for China, *Journal of Geodesy*, 96(6), doi:10.1007/s00190-022-01630-z.

575 Zhang, H., Y. Yuan, W. Li, B. Zhang, and J. Ou (2017), A grid-based tropospheric product for China using a GNSS network, *Journal of Geodesy*, 92(7), 765-777, doi:10.1007/s00190-017-1093-z.

Zheng, F., Y. Lou, S. Gu, X. Gong, and C. Shi (2017), Modeling tropospheric wet delays with national GNSS reference network in China for BeiDou precise point positioning, *Journal of Geodesy*, 92(5), 545-560, doi:10.1007/s00190-017-1080-4.

580 Zheng, Y., C. Lu, Z. Wu, J. Liao, Y. Zhang, and Q. Wang (2022), Machine Learning-Based Model for Real-Time GNSS Precipitable Water Vapor Sensing, *Geophysical Research Letters*, 49(3), doi:10.1029/2021gl096408.

Zhou, Y., Y. Lou, W. Zhang, C. Kuang, W. Liu, and J. Bai (2020), Improved performance of ERA5 in global tropospheric delay retrieval, *Journal of Geodesy*, 94(10), doi:10.1007/s00190-020-01422-3.

Zhou, Y., Y. Lou, W. Zhang, P. Wu, J. Bai, and Z. Zhang (2022), WTM: The Site-Wise Empirical Wuhan University Tropospheric Model, *Remote Sensing*, 14(20), 5182, doi:10.3390/rs14205182.

585 Zhu, G., Huang, L., Yang, Y. et al. Refining the ERA5-based global model for vertical adjustment of zenith tropospheric delay. *Satell Navig* 3, 27 (2022). <https://doi.org/10.1186/s43020-022-00088-w>